

Comparison of tensile properties between the NiFeCoCr high-entropy alloys

Jiale Man ^{a,b}, Baolin Wu ^{a,*}, Guosheng Duan ^a, Lu Zhang ^a, Yandong Liu ^b, Claude Esling ^c

^a School of Materials Science and Engineering, Shenyang Aerospace University, 110136, Shenyang, China

^b Key Laboratory for Anisotropy and Texture of Materials (Ministry of Education), Northeastern University, 110819, Shenyang, China

^c LEM3 UMR CNRS 7239, Université de Lorraine, 57045, Metz, France



ARTICLE INFO

Keywords:

High entropy alloy
Solid-solution strengthening
Strain hardening rate
Strength-ductility
Lomer-cottrell lock

ABSTRACT

In this study, four NiFeCoCr high-entropy alloys were prepared with different molar ratios. The tensile properties were investigated and discussed. The results showed that adjusting the elemental proportions for solid-solution strengthening is inefficient, because the atomic radius mismatch/misfit volume, Burgers vector magnitude, shear modulus and shear modulus mismatch are quite similar in the different molar ratio alloys. The grain refinement enhances the yield strength effectively, but has limited impact on the strain hardening rate and ductility. The NiFe₂CoCr and NiFe₂CoCr alloys exhibit higher ductility than the NiFeCoCr and Ni₂FeCoCr alloys due to the higher strain hardening rate. The higher strain hardening rate of the NiFe₂CoCr and NiFe₂CoCr alloys dominantly results from the forest dislocation strengthening promoted by the activated stacking faults with Lomer-Cottrell locks.

1. Introduction

FCC-structured high/medium-entropy alloys (H/MEAs) have been extensively investigated due to their high performances for potential applications [1–8]. These alloys usually exhibit high ductility but low strength. Consequently, many researches have been focused on strengthening to develop HEAs/MEAs with superior strength-ductility synergy [9–15]. Constructing a heterogeneous microstructure via thermos-mechanical processing is an effective pathway. The results showed that the tensile yield strength can reach as high as 2.0 GPa with an elongation larger than 10% [16–18]. However, the strength-ductility synergy of this kind of alloys is significantly related to the molar ratio between principal elements that determine the characteristics of solid-solution matrix. Therefore, it is quite important to concern the characteristics of the solid-solution phase for the alloys design.

Actually, what physical mechanisms or parameters controlling strength and ductility of a solid-solution alloy is an interesting topic on the HEAs/MEAs design. Earlier, the solution hardening in a single solid-solution phase alloy was referred to the elastic interaction between dislocations and solutes [19]. Fleischer [20] indicated that this kind of interaction depends mainly on the atomic radius mismatch, shear modulus, and shear modulus mismatch. Accordingly, a theoretical strengthening model was established [21]. Based on this model, Senkov et al. [22] proposed an empirical model that is suitable for HEAs. In

theory, Varvenne et al. [23,24] developed a model in terms of dislocation interactions with the random local concentration fluctuations around the average composition, which was validated against molecular simulations, exhibiting a good quantitative agreement to the experimental results. Further, Maresca et al. established a theoretical model that is suitable for BCC-structured HEAs [25]. In the latter model, various parameters such as vacancy formation energy E_v or self-interstitial formation energy E_i , Burgers vector b (determined by lattice constant a), and the dislocation kink length ζ_c (associated with characteristic energy fluctuations $\Delta\tilde{E}_p$) collectively contribute to the strengthening of the alloys. Aforementioned models clearly presented the relationships between strength and related parameters. However, different models cover different parameters in the each perspective. The effect of related parameters on strength is comprehensive and complex. Limited to the insufficient information in physical metallurgy at present, the relationship between strength and related parameters has been yet vague. In fact, some aforementioned parameters have relations between each other.

Usually, the increase of the yield strength companies with a drop of ductility. This seems a common regulation in a kind of alloys. However, many researches showed that the yield strength and ductility can synergistically increase [26–29]. This indicates that the parameters or factors influencing ductility are uncertainly contradictory to strengthening alloys. For enhancing the strength-ductility synergy, the key point

* Corresponding author. School of Materials Science and Engineering, Shenyang Aerospace University, South Avenue of Daoyi, 110136, Shenyang, China.
E-mail address: wubaolin@sau.edu.cn (B. Wu).

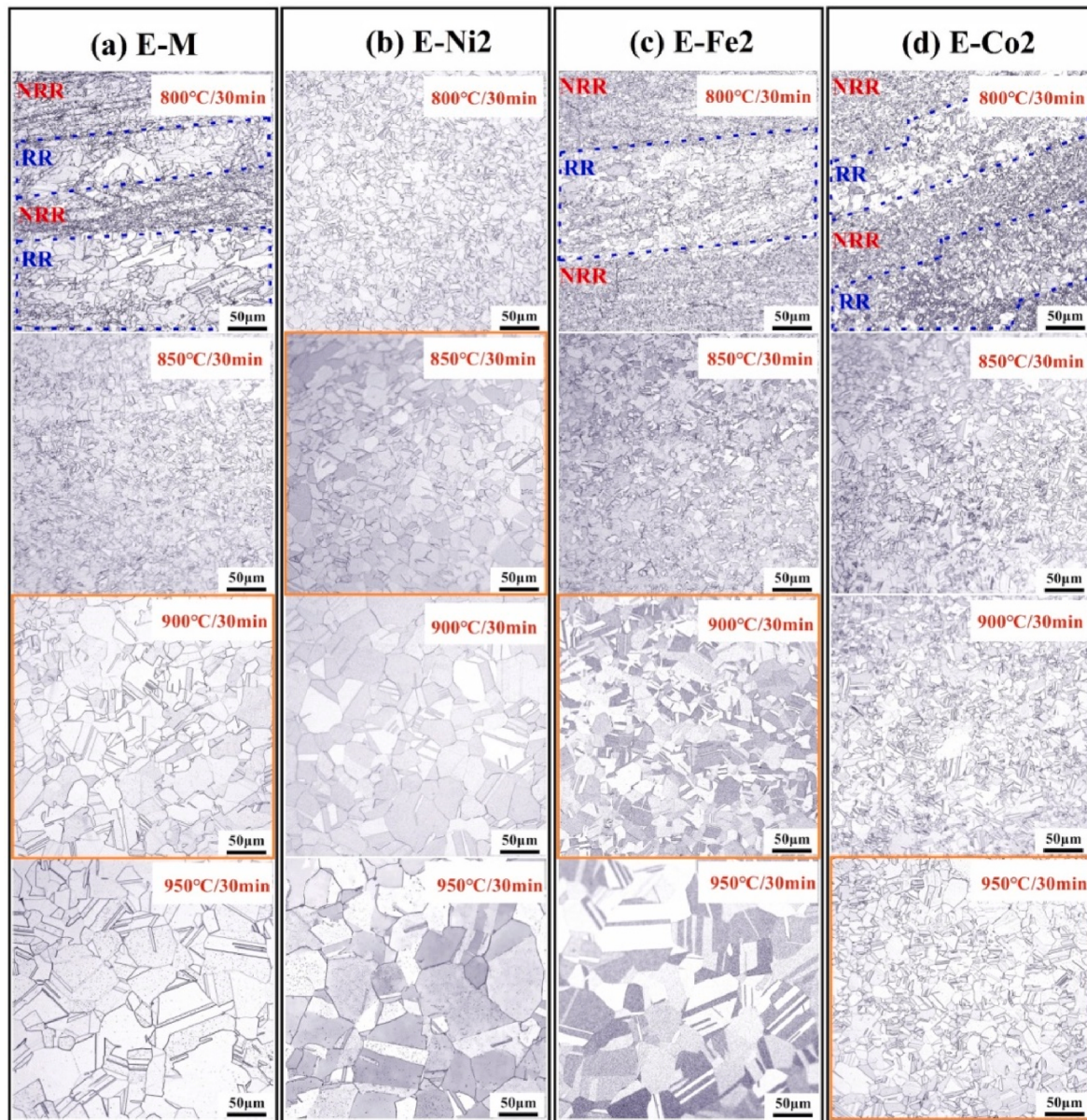


Fig. 1. Optical microstructures of the annealed plates at different temperatures. (a) the E-M alloy; (b) the E-Ni2 alloy (c): the E-Fe2 alloy (d): the E-Co2 alloy.

is to control independent parameters or factors for a strength-ductility balance, in which the influencing parameters on ductility need to be also clarified. Revealing the relationship between the mechanical properties and related parameters is of interest. In this study, four NiFeCoCr HEAs with different molar ratios were prepared. The tensile properties were investigated and discussed in terms of physical parameters. The results serve as a reference for designing FCC-structured MEAs with desirable solid-solution matrix.

2. Experimental

The alloys were prepared based on raw metals of Ni, Fe, Co and Cr with purities higher than 99.9 %. The molar ratio Ni:Fe:Co:Cr was expressed as NiFeCoCr, Ni₂FeCoCr, NiFe₂CoCr and NiFeCo₂Cr, denoted with E-M, E-Ni2, E-Fe2 and E-Co2, respectively. These alloys were prepared by arc-melting through 6 times under an argon atmosphere, and subsequently homogenized in vacuum at 1200 °C for 12h, followed by water quenching (WQ). Plate samples with dimensions 40mm × 15mm × 7.5 mm were extracted from these ingots, and then cold-rolled at room

temperature with a thickness reduction of 80 % (from 7.5 mm to 1.5 mm). These cold-rolled plates were annealed at 800 °C, 850 °C, 900 °C and 950 °C, respectively, for 30min, and then were cooled by WQ.

Tensile samples were cut out of the annealed plates with the tensile direction parallel to the rolling direction (RD) by an electro-discharge machine. The gauge length was 18.0 mm with the cross-section sizes of 4.0 mm × 1.5 mm. The tensile tests were conducted on a CMT-5305GL universal electronic tensile testing machine with a strain rate of $1 \times 10^{-3} \text{ s}^{-1}$ at room temperature. Five samples were used in characterizing the tensile properties of each plate. The results were averaged.

Initial microstructures of the annealed plates were observed under the optical microscope. To characterize plastic deformation microstructures of the tensile samples, observations were carried out on the longitudinal section under scanning electron microscope (SEM)-electron back-scattered diffraction (EBSD) (Zeiss-Sigma). The specimens for the SEM-EBSD observation were initially ground by 3000-grit SiC paper, then electrochemically polished for the final surface clarification using a HClO₄:C₂H₆O = 1:9 solution with a direct voltage of 28V at room temperature. To further reveal microstructures, transmission electron

Table 1

The averaged tensile yield strength ($\sigma_{0.2}$) and elongation (EL) of the alloys.

Alloy denotation	Heat treatment	Average diameter	$\sigma_{0.2}$ (MPa)	EL (%)	Average hardening rate
E-M	850 °C/30min	8.42	356.2	66.3	13.6
	900 °C/30min	26.88	332.6	59.2	13.6
	950 °C/30min	59.24	287.1	58.3	13.0
E-Ni2	800 °C/30min	4.36	358.5	56.6	13.5
	850 °C/30min	10.72	329.1	53.9	13.5
	900 °C/30min	32.75	317.6	52.9	13.5
	950 °C/30min	40.79	266.4	52.8	14.0
E-Fe2	850 °C/30min	8.28	392.6	62.4	15.7
	900 °C/30min	13.49	341.6	61.2	15.9
	950 °C/30min	60.44	316.2	60.7	15.5
E-Co2	850 °C/30min	3.84	454.3	67.4	18.2
	900 °C/30min	8.16	401.6	66.6	19.2
	950 °C/30min	11.49	361.4	65.5	18.1

microscope (TEM) observations were carried out using the JEM-2100F instrument. TEM specimens were primarily punched to $\Phi 3$ mm plate sheets and then mechanically ground to about 55 μm in thickness, followed by Ion-milling.

3. Results

3.1. Initial microstructures

Fig. 1 shows initial microstructures of the annealed plates under the optical observation. After annealed at 800 °C for 30min, E-M (Fig. 1 (a)), E-Fe2 (Fig. 1 (c)) and E-Co2 (Fig. 1 (d)) alloys exhibited a microstructure that was not completely recrystallized, containing both recrystallized regions (RRs) and non-recrystallized regions (NRRs). In contrast, alloy E-Ni2 exhibited a completely recrystallized microstructure. Annealed at 850 °C, all the alloys were completely recrystallized. It can be seen that grain size of the alloys increased with the increase of annealing temperature. Comparatively, recrystallization process in the E-Ni2 alloy was faster, whereas it was slowest in the E-Co2 alloy. So, the E-Co2 alloy had smallest grain size among the alloys under the same heat treatment condition. Numerous annealing twins can be observed in the alloys.

3.2. Tensile behaviors

The averaged tensile properties of the completely recrystallized alloys are listed in Table 1. The typical engineering stress-strain curves are shown in Fig. 2. It can be seen that the alloys had low yield strength $\sigma_{0.2}$ (266 MPa~454 MPa) and high elongation (EL) (53 %–67 %). From Fig. 2, It is seen that the flow stress elevates with the decrease of grain size for all the alloys. However, the effect of grain size on ductility was limited for the same alloy. In overall, the ductility of alloy E-Co2 was the highest among the alloys. The refinement of grains can effectively induce dislocation piling up at grain boundaries, favorable for strain hardening. The strain hardening rates were calculated according to the true stress-strain curves and are listed in Table 1. We can see that the strain hardening rate was similar in the same alloy with different grain size. In overall, the strain hardening rate was also the highest in the E-Co2 alloy. With the similar grain size, the E-Co2 alloy (annealed at 900 °C) exhibited much higher strain hardening rate than alloys E-Fe2

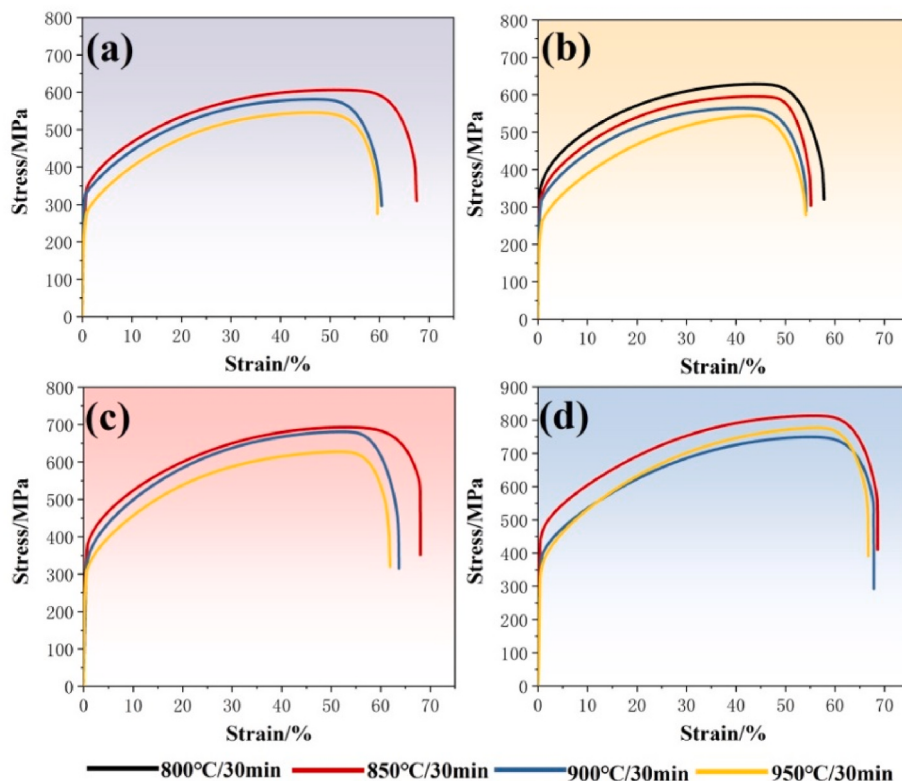


Fig. 2. Engineering tensile stress-strain curves of the annealed plates at different temperatures.

(a) the E-M alloy; (b) the E-Ni2 alloy (c): the E-Fe2 alloy (d): the E-Co2 alloy.

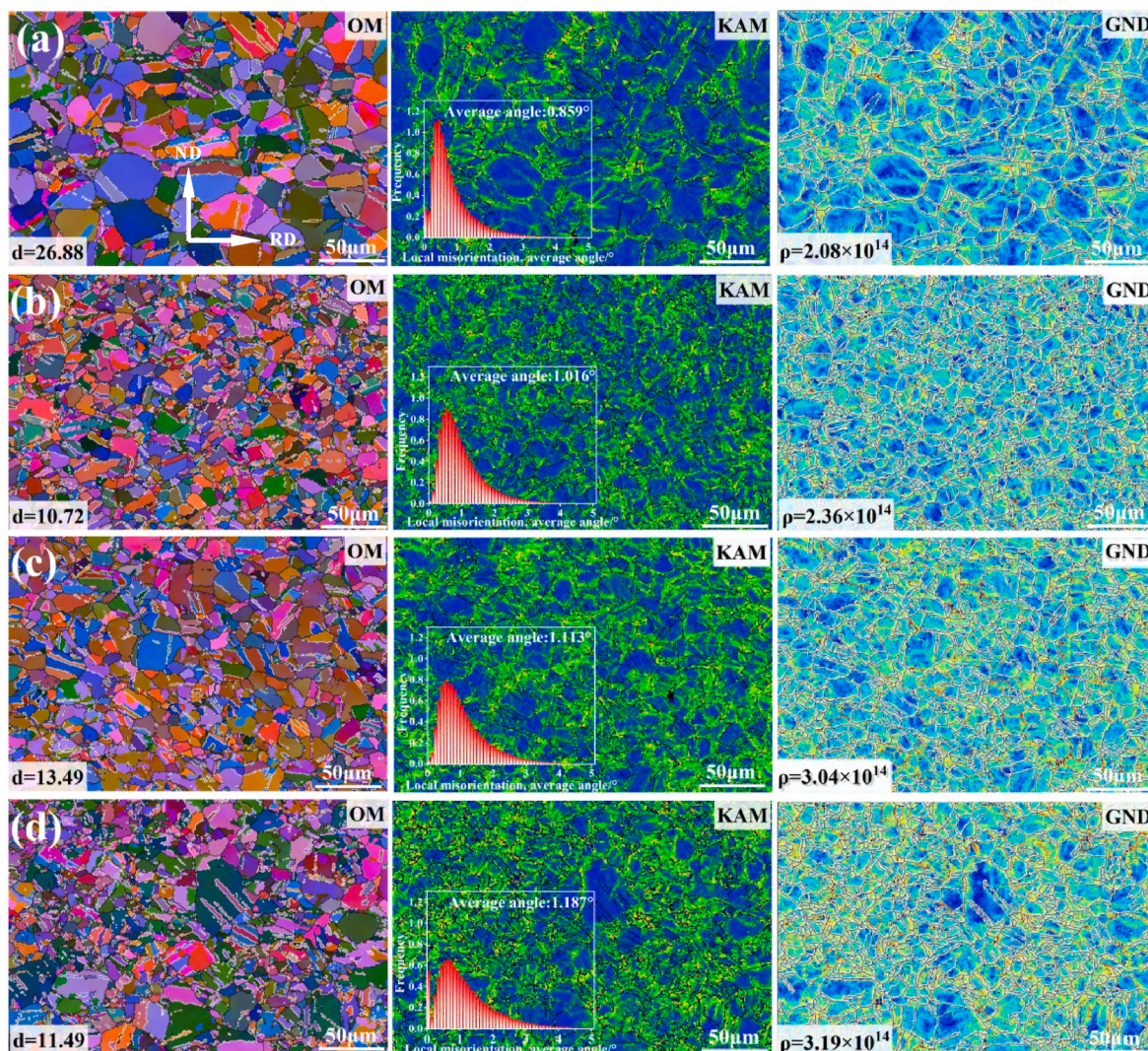


Fig. 3. OM, KAM and GND maps of the tensile samples of the alloys strained to $\sim 11\%$. (a) the E-M alloy annealed at $900\text{ }^{\circ}\text{C}/30\text{min}$; (b) the E-Ni2 HEA annealed at $850\text{ }^{\circ}\text{C}/30\text{min}$; (c) the E-Fe2 annealed at $900\text{ }^{\circ}\text{C}/30\text{min}$; (d) the E-Co2 annealed at $950\text{ }^{\circ}\text{C}/30\text{min}$.

(annealed at $850\text{ }^{\circ}\text{C}$) and E-M (annealed at $850\text{ }^{\circ}\text{C}$). The strain hardening rate of alloy E-M was the lowest. Annealed at $950\text{ }^{\circ}\text{C}$, the hardening rate of the E-Co2 alloy was also much higher than the E-Fe2 (annealed at $900\text{ }^{\circ}\text{C}$) and E-Ni2 (annealed at $850\text{ }^{\circ}\text{C}$) alloys with similar grain size (see Table 1). This suggests that there exist other factors influencing the strain hardening rate.

3.3. Deformed microstructures

To reveal the difference of deformed microstructures between these alloys, SEM-EBSD observations were conducted on the tensile samples that were strained to a total strain of $\sim 11\%$. Fig. 3 presents EBSD orientation-maps (OMs), Kernel average misorientation (KAM) maps and geometry necessary dislocation (GND) maps of the tensile samples of the alloys. KAM is defined as the average misorientation between each measurement point and all immediate neighbors, which induces lattice curvature [30]. During plastic deformation, stored dislocations can be divided into two classes termed statistically stored dislocations (SSDs) and geometrically necessary dislocations (GNDs), respectively [31,32]. SSDs, resulting from the random trapping of mobile dislocations, are homogeneously distributed within materials and can convert to GNDs in further deformation. GNDs have a net non-zero Burgers vector and contribute to the lattice curvature that can be estimated by KAM

characterization under EBSD. In general, most stored dislocations in a severe deformation can be considered as GNDs which accommodate long-range strain gradient [32].

From Fig. 3, it is seen that GNDs featured a low density within the coarse grains, concentrating mainly near grain boundaries in the E-M alloy (Fig. 3 (a)). The average density ρ of GNDs in the E-M alloy was $2.08 \times 10^{14} (1/\text{m}^2)$. In the other alloys with smaller grain size, GNDs expanded into the interior of grains in addition to concentrating near grain boundaries. With similar grain sizes, alloys E-Ni2 (Fig. 3 (b)), E-Fe2 (Fig. 3 (c)) and E-Co2 (Fig. 3 (d)) exhibited different GND densities with values of $2.36 \times 10^{14} (1/\text{m}^2)$, $3.04 \times 10^{14} (1/\text{m}^2)$ and $3.19 \times 10^{14} (1/\text{m}^2)$, respectively. The GND density increased significantly in the alloys with fine grains, but the grain size was not the only parameter determining the GND density. With increasing GND density, both the average misorientation and maximum misorientation increased. Generally, low GND density is conducive to reducing stress concentration. High GND density is favorable for strain hardening in terms of dislocation pinning during slip.

Textures of the tensile sample are shown in Fig. 4. Textures in the E-M (Fig. 4 (a)), E-Ni2 (Fig. 4 (b)) and E-Fe2 (Fig. 4 (c)) alloys were featured by the α and β orientation fibers covering Goss (G, $\{110\} < 001 >$), Brass (B, $\{110\} < 112 >$), Copper (C, $\{112\} < 111 >$) and S ($\{123\} < 634 >$) components. In addition, a weak rotation Cube (R Cube,

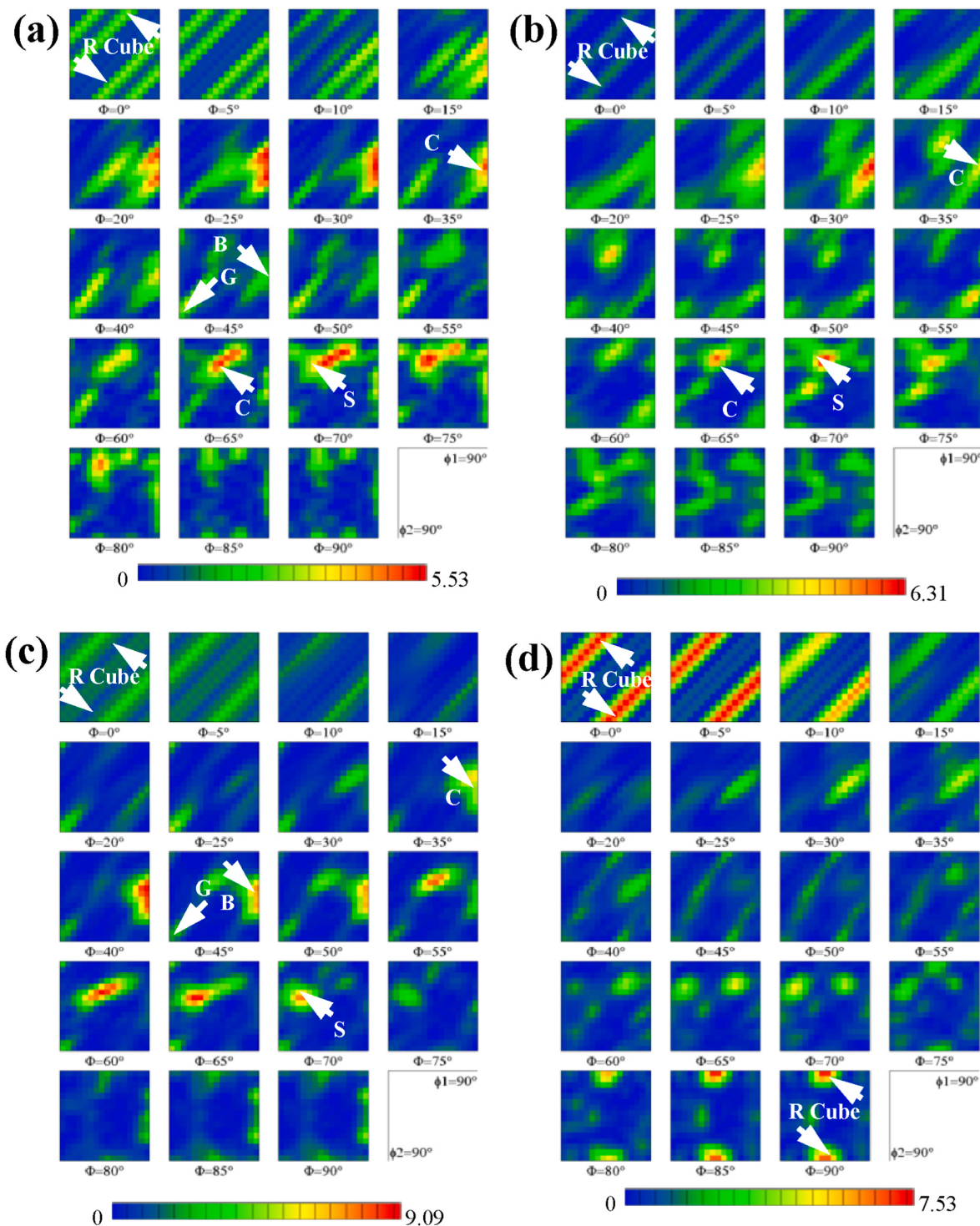


Fig. 4. Orientation distribution function (ODF) maps of constant φ sections ($\Delta\varphi = 5^\circ$).
(a) the E-M alloy; (b) the E-Ni₂ alloy (c): the E-Fe₂ alloy (d): the E-Co₂ alloy.

{001}<110>) component was also contained in these alloys. G, B, C and S components have been usually found in the cold-rolled FCC-structured alloys with high stacking fault energy, such as aluminum alloys, copper alloys, and stainless steels. Previous research indicated that the cold-rolled CoCrFeMnNi high entropy alloys with low stacking fault energy also featured these components, as reported in Refs. [33–35]. After annealing, the deformation texture components are usually retained and reduced in density [36–38]. The similarity in the nature of the texture to the deformed can be explained in terms of oriented nucleation during

recrystallization in shear bands where nuclei of recrystallized grains of particular orientations form at or near the deformed regions of same or similar orientations [38]. With few Goss and S orientations, the recrystallization textures in shear bands appear to be weak during annealing. Annealing twins in FCC crystals contribute to weak textures during annealing as well. The E-Co₂ alloy dominantly featured the rotation Cube component (Fig. 4 (c)) which was much higher in density than that in the other alloys. The formation of rotation Cube component was referred to annealing twins [39]. Although there were some

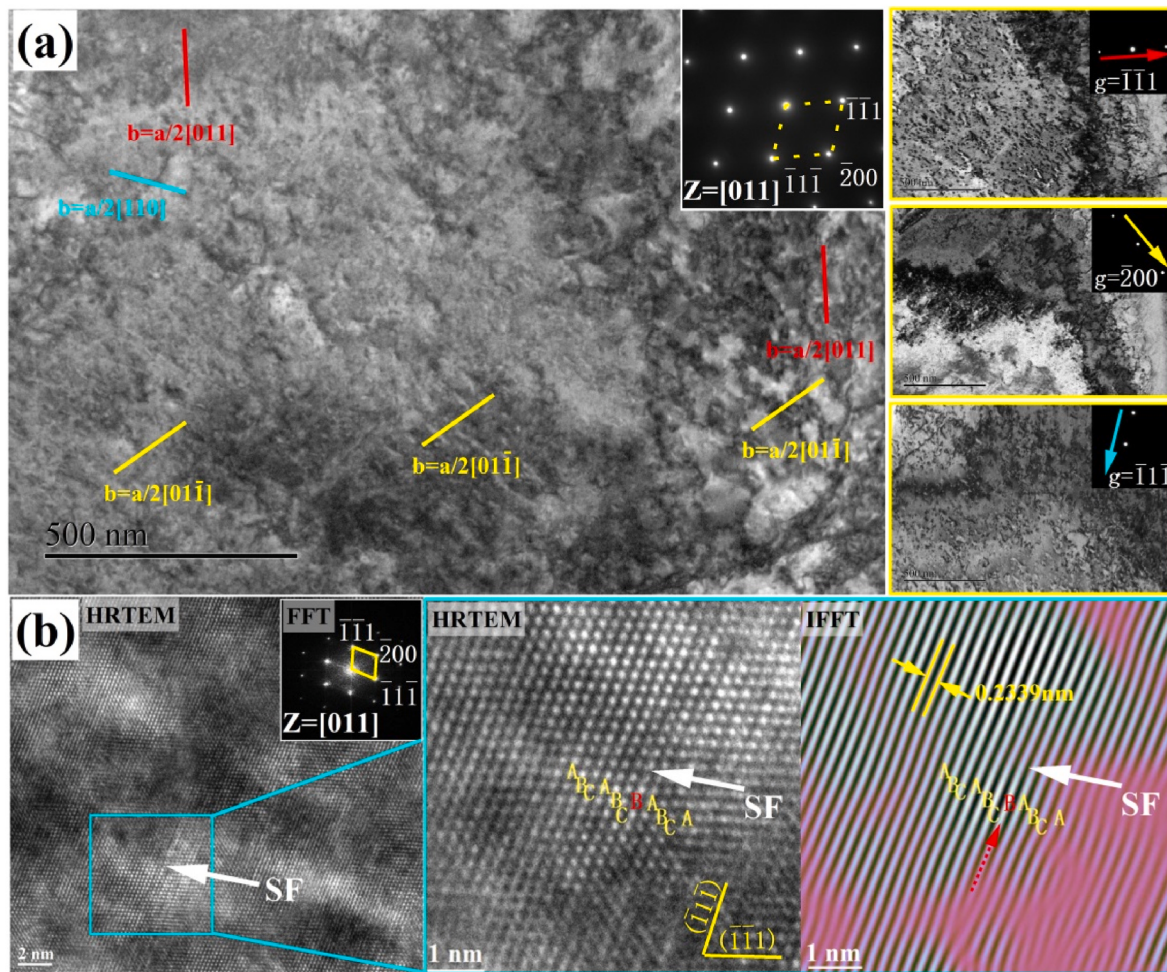


Fig. 5. TEM bright field images of the E-M alloy sample tensioned to 11 % total strain (a), and HRTEM images showing an extrinsic stacking fault (b).

differences between the alloys in texture component and density, the calculated Taylor factor M was 3.10, 3.09, 3.20 and 3.19, respectively, close to each other for E-M, E-Ni2, E-Fe2 and E-Co2 alloys.

Fig. 5 (a) shows bright field (BF) TEM images of the E-M alloy tensioned to a total strain of 11 %. With the same incident axis [011], the corresponding BF images under the 3g beam diffraction conditions are shown on the right side of the figure. The reciprocal vector g is represented by arrows with different colors. Burgers vector b was identified according to the $g \cdot b = 0$ criterion, and is marked with solid lines that represents both the forward and reverse directions. Dislocations correspond to the Burgers vector of $b = a/2[01-1]$, $b = a/2[011]$ and $b = a/2[110]$, respectively. Dislocations characterized with different Burgers vectors indicate that multiple slip systems were activated in the deformation. Under the HRTEM observation, some stacking faults (SFs) can be identified according to the inverse fast Fourier transform (IFFT) image, as seen in Fig. 5 (b). CoCrFeNi-based HEAs have usually low stacking fault energy that easily results in the decomposition of an unit-dislocation by $1/2<110> \rightarrow 1/6<211> + 1/6<12-1>$, generating a SF that consists of a pair of Shockley partial dislocations [40,41]. In the IFFT image, the lattice was severely distorted in the areas with pink color.

Fig. 6 (a) presents BF-TEM images of the E-Ni2 alloy tensioned to the total strain of 11 %. Most dislocations correspond to the Burgers vector $b = a/2[011]$, $b = a/2[101]$ and $b = a/2[10-1]$, respectively. Similarly, the multiple slip systems were activated in this alloy. The HRTEM image and the corresponding IFFT images (Fig. 6 (b)) show plentiful dislocations on (-111) or ($1-11$) atomic planes, distributing in the distorted lattice. No stacking fault was found in this alloy.

Fig. 7 presents BF-TEM images of the M-Fe2 alloy tensioned to the total strain of 11 %. In addition to unit-dislocations resulting from multiple slip systems (Fig. 7 (a)), plentiful SFs can be found, as seen from the HRTEM image and R1 and R2 magnified IFFT images in Fig. 7 (b). Unlike the unit-dislocation which can crossly slip, the partial dislocations can only slide in a co-planar mode. When the partial dislocations from different slip systems encounter each other, a Lomer-Cottrell (L-C) lock could form via $1/6<-21-1> + 1/6<1-12> \rightarrow 1/6<-101>$. In the HRTEM image (Fig. 7 (b)), we can see that SFs on ($-11-1$) and ($-1-11$) atomic planes construct some L-C locks, indicated by a red circle as an example.

The tensioned (11 % total strain) E-Co2 alloy also exhibited multiple slip systems during plastic deformation, as seen in the BF-TEM images (Fig. 8 (a)). On ($-11-1$) and ($-1-11$) atomic planes, SFs can be found in the HRTEM image and IFFT images in Fig. 8 (b). The partial dislocations of SFs on the ($-11-1$) and ($-1-11$) atomic planes interacted to form L-C locks. As shown in the IFFT images, SFs on the ($-11-1$) and ($-1-11$) atomic planes featured the extrinsic and intrinsic types, respectively. A L-C lock is indicated by a red circle, showing the partial dislocations interaction.

Summarily, multiple slip systems were activated in all the investigated alloys during tension. This is the slip characteristics in FCC-structured HEAs which is favorable for ductility. However, the alloys exhibited quite different configurations of dislocations. In comparison, the E-Co2 and E-Fe2 alloys exhibited more SFs than the E-M alloy, forming L-C locks during the co-planar slip. The E-Ni2 alloy was mainly deformed by the unit-dislocation slip. This suggests that the E-Co2 and E-Fe2 alloys had lower stacking fault energy than the E-M and E-Ni2

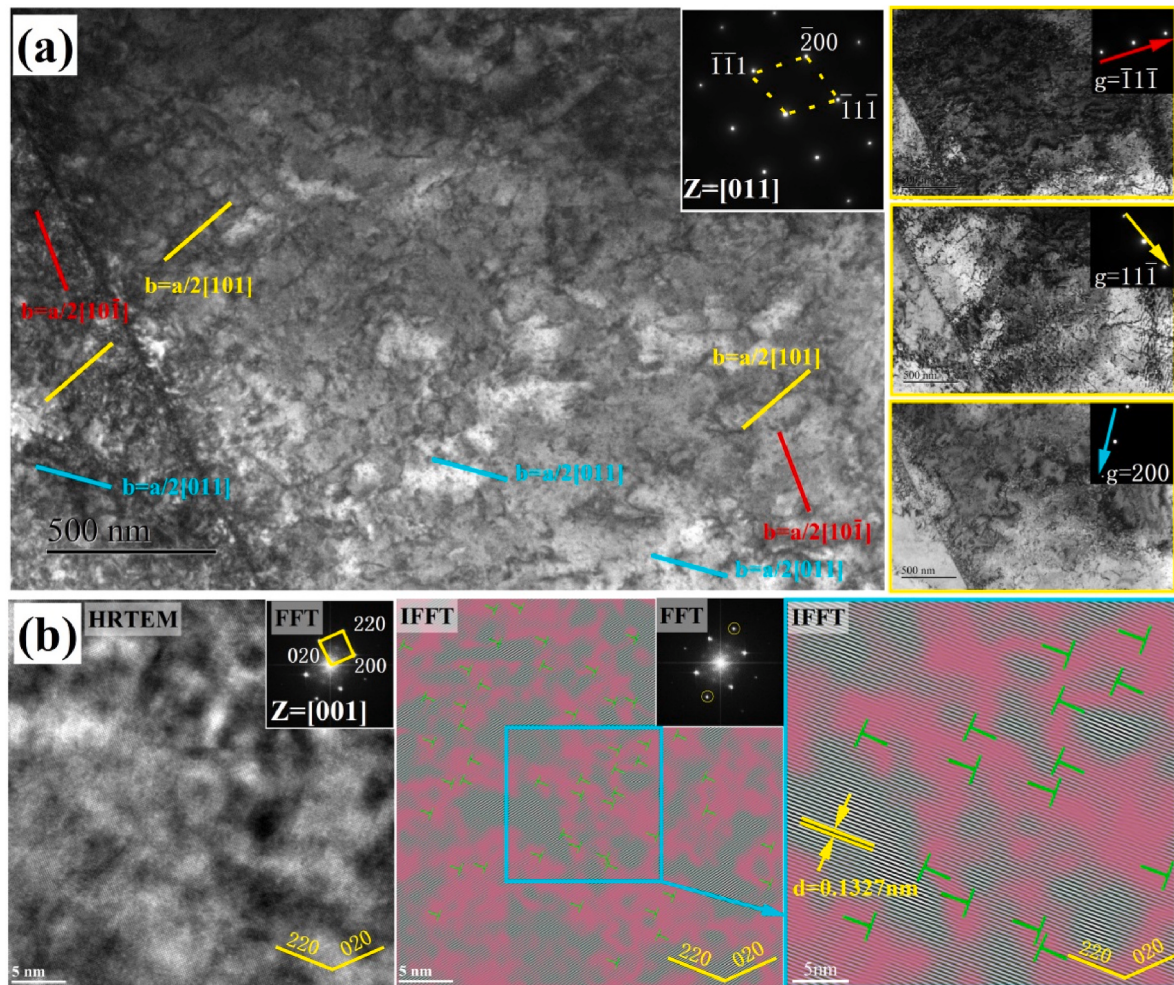


Fig. 6. BF-TEM images (a) of the E-Ni2 alloy sample tensioned to 11 % total strain, and the HRTEM image (b) with the corresponding IFFT images at the right side.

alloys.

4. Discussion

4.1. Strengthening

From the experimental results, it is seen that the yield strength increases with decreasing grain size for the same alloy. The results are well consistent with the Hall-Petch relationship. The yield strength vs. grain size are presented in Fig. 9. With the similar gain sizes, there is a little difference of the yield strengths between the different alloys. According to the Senkov [22] and Varvenne [23,24] models, the yield strength could be affected by some physical parameters in addition to grain size.

The yield strength $\sigma_{0.2}$ of current alloys are contributed by three parts including the lattice resistance, solid-solution strengthening and grain boundary strengthening, expressed as:

$$\sigma_{0.2} = \sigma_0 + \Delta\sigma_{ss} + kd^{-\frac{1}{2}} \quad (1)$$

where σ_0 represents the lattice resistance; $\Delta\sigma_{ss}$ represents the solid-solution strengthening; d represents the average grain diameter; k is a constant in the Hall-Petch relationship. The lattice resistance is represented by the Peierls-Nabarro relation:

$$\sigma_0 = \frac{2G}{1-\nu} \exp\left(-\frac{2\pi d_0}{b(1-\nu)}\right) \quad (2)$$

where a is the lattice constant; ν is Poisson ratio; d_0 is the interspacing of

slip planes. To estimate the solid-solution strengthening, we used the Senkov and Varvenne models, respectively. The Senkov model is expressed as [22]:

$$\sigma_{ss} = AG \left[\sum_i e_i^2 x_i \right]^{2/3} \quad (3)$$

where A is the fitting constant; $G = \sum_i x_i G_{ii}$, x_i is the molar fraction of element i , and G_{ii} is the shear modulus of pure metal of element i . In Eq. (3),

$$\varepsilon_i = \left[\left(\frac{\eta_i}{1 + 0.5|\eta_i|} \right)^2 + \alpha^2 \delta_i^2 \right]^{0.5} \quad (4)$$

$$\eta_i = \frac{n}{m} \sum_j x_j \delta G_{ij} \quad (5)$$

$$\delta_i = \frac{n}{m} \sum_j x_j \delta R_{ij} \quad (6)$$

where η_i is the shear modulus mismatch of pure metal i to other pure metals; δ_i is the atomic radius mismatch of element i to other elements; m (12 for the FCC structure) is the coordination number, and n (13 for the FCC structure) is the number of atoms in a dense cluster; α is the constant depending on the dislocation type (it is usually assumed that $3 < \alpha < 16$ for screw dislocations and $\alpha > 16$ for edge dislocations); $\delta G_{ij} = \frac{2(G_{ii} - G_{jj})}{G_{ii} + G_{jj}}$,

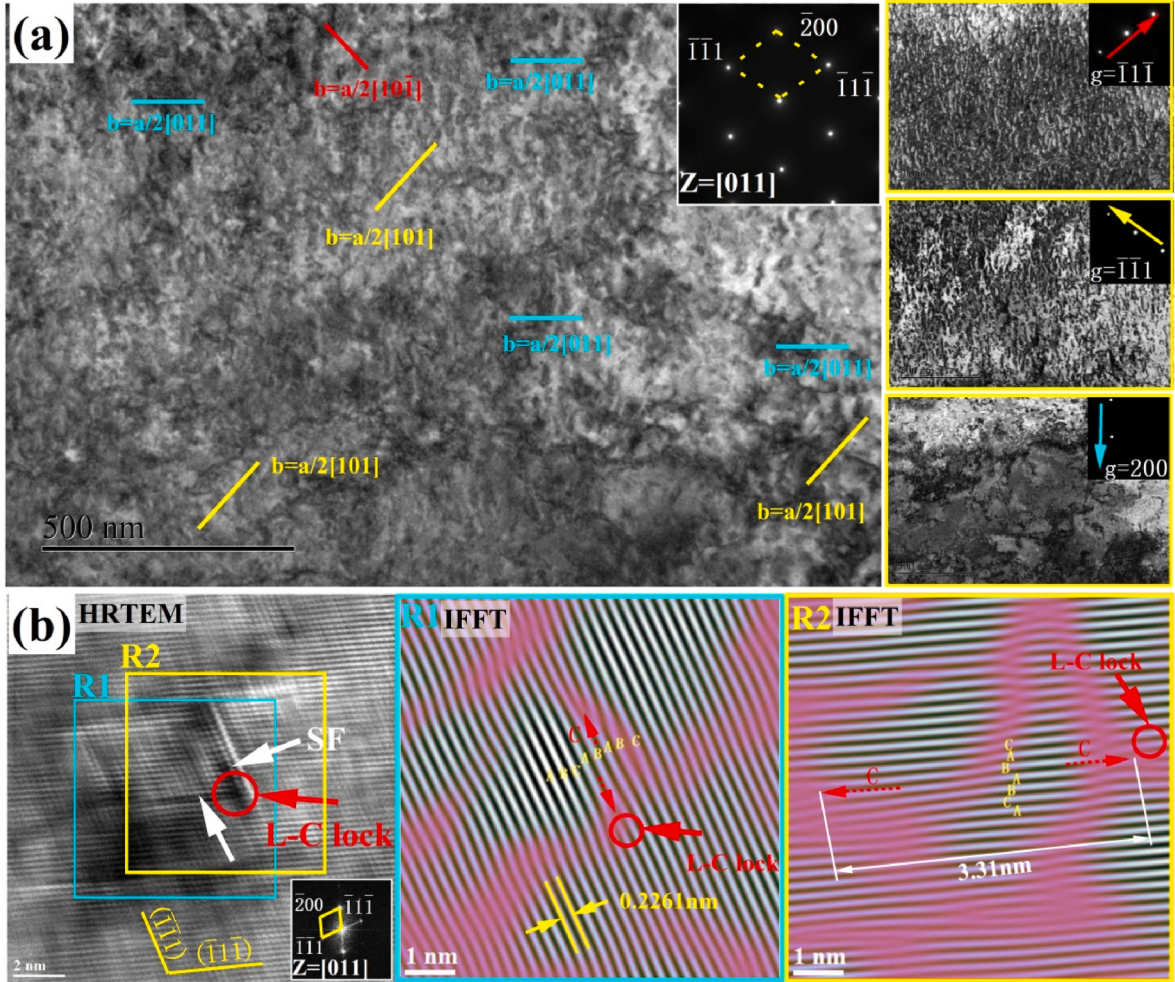


Fig. 7. BF-TEM images of the M-Fe2 alloy sample tensioned to 11 % total strain, and the HRTEM image (b) with the corresponding IFFT images at the right side. The stacking faults and L-C locks can be found.

$\delta R_{ij} = \frac{2(R_{ii} - R_{jj})}{R_{ii} + R_{jj}}$, where R_{ii} is the distance between the nearest balanced atoms or atomic radius of pure metal i . According to this model combined with Eq. (1), we calculated the yield strength of the alloys at all states. In the calculation, the constants A and α were taken as 1.54×10^{-4} and 18, respectively, for all the alloys at different states. The average k value was 353 according to Fig. 9. The Poisson ratio ν was averaged and taken as 0.283 according to the values of the pure metals. The calculated parameters are listed in Table 2 and Table 3.

According to the Varvenne model, the yield stress induced by thermal activation can be simplified as [42]:

$$\tau_y(T, \dot{\varepsilon}) = \tau_{y0}(T) \left[1 - \left(\frac{kT}{\Delta E_b(T)} \ln \frac{\dot{\varepsilon}_0}{\dot{\varepsilon}} \right)^{\frac{2}{3}} \right] \quad (7)$$

where

$$\tau_{y0} = 0.01785 \alpha^{\frac{1}{3}} \bar{\mu} \left(\frac{1 + \bar{\nu}}{1 - \bar{\nu}} \right)^{\frac{4}{3}} \left[\frac{\sum_n C_n \Delta V_n^2}{b^6} \right]^{\frac{2}{3}} \quad (8a)$$

and

$$\Delta E_b = 1.5618 \alpha^{\frac{1}{3}} \bar{\mu} b^3 \left(\frac{1 + \bar{\nu}}{1 - \bar{\nu}} \right)^{\frac{2}{3}} \left[\frac{\sum_n C_n \Delta V_n^2}{b^6} \right]^{\frac{1}{3}} \quad (9a)$$

In the above equations, $\bar{\mu}$ and $\bar{\nu}$ represent weighted shear modulus and Poisson ratio for the random alloys, respectively; ΔV_n denotes the

misfit volume of element n in random alloys, $\Delta V_n = V_n - \sum_n c_n V_n$, $V_n = a_n^3/4$, where a_n is FCC lattice constant of pure elements; C_n represents the concentration of element n ; b is Burgers vector magnitude, and α' is a constant related to the dislocation line tension, usually taken as 0.123. To fit the present results, we modified the coefficient of 0.01785 to 0.00108 in Eq. (8). Burgers vector magnitude b was determined according to the measured lattice constant a by XRD. The parameters related to the Varvenne model are listed in Table 4.

Fig. 10 presents the comparison of the yield strength between the experimental and calculated results by the Senkov and Varvenne models, respectively, where the contributions by the lattice resistance σ_0 , solid-solution strengthening $\Delta\sigma_{ss}$ and grain boundary strengthening $kd^{-1/2}$ are also included in. It can be seen that the calculated results of the yield strength are basically in line with the experimental results, with a certain deviation. The result given by the Varvenne model has a slight higher accuracy than that given by the Senkov model. The strengthening effect is mainly contributed by the grain refinement. The lattice resistance σ_0 and solid-solution strengthening $\Delta\sigma_{ss}$ vary slightly in the different alloys. The difference is limited due to the fact that the atomic radius mismatch/the misfit volume, Burgers vector magnitude, shear modulus and shear modulus mismatch are quite similar in the different alloys. This indicates that adjusting elemental proportions in the solid-solution is inefficient for strengthening this kind of alloys. Grain refinement is a significant pathway to enhance the alloys. Nevertheless, adjusting elemental proportions can lead to a significant impact on the strain hardening rate.

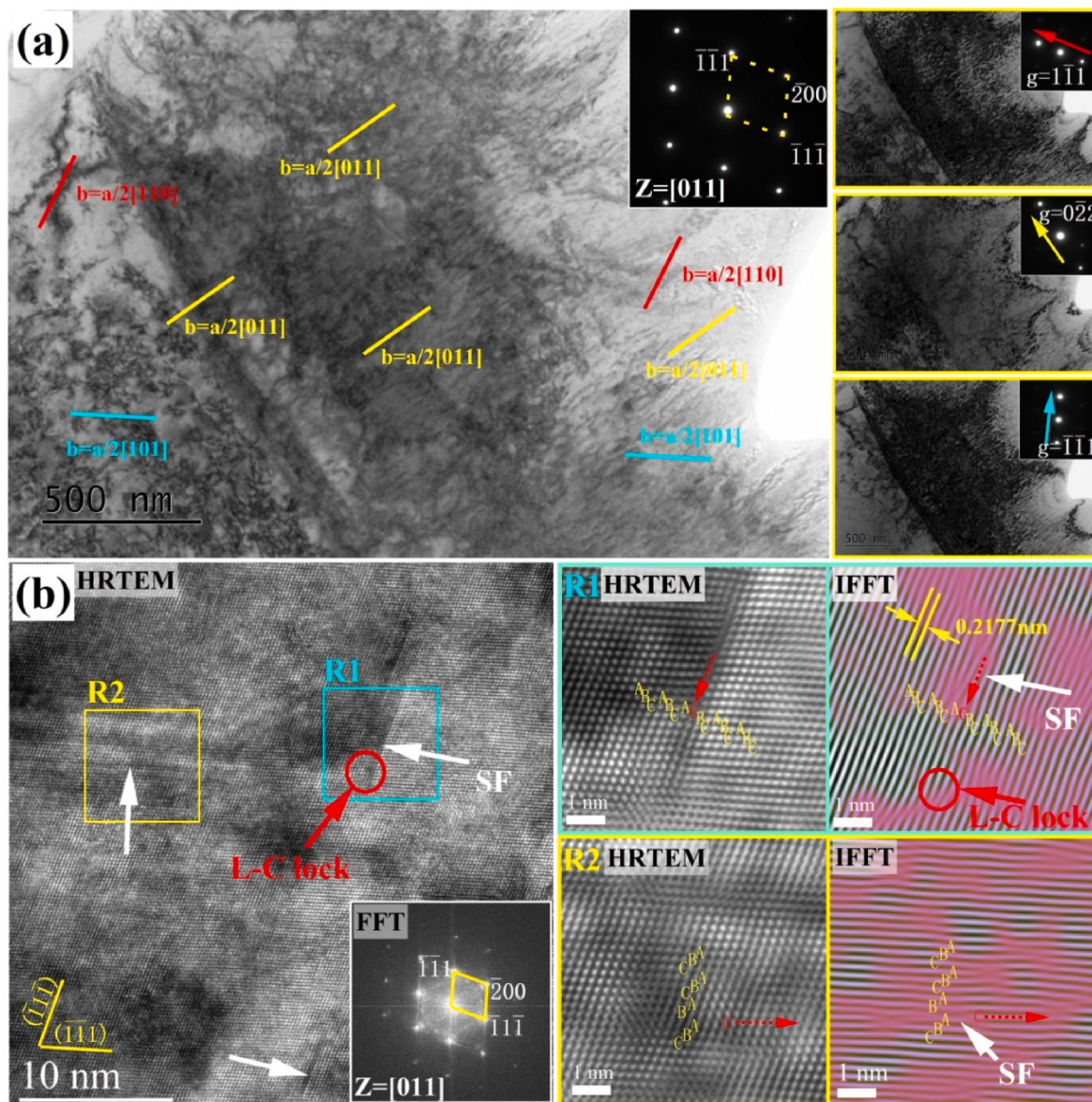


Fig. 8. TEM BF images (a) of the E-Co₂ alloy sample tensioned to 11 % total strain, and HRTEM images (b) with the corresponding IFFT images at the right side. The stacking faults and L-C locks can be found.

4.2. Strain hardening rate

Fig. 11 (a) presents the true stress-strain curves of the alloys. The strain hardening rate in the alloy E-Co₂ alloy was the highest, and it was much lower in the E-M and E-Ni₂ alloys. Fig. 11 (b) presents the true stress-strain curves during tension in a loading-unloading-reloading (LUR) manner. The LUR cyclic tensile test has been usually conducted to characterize the evolution of flow stress partition and figure out the strain-hardening rate [43,44], in which the evolution of back stress and effective stress can be compared during tensile deformation. As a strengthening mode, back stress is related to various factors such as characteristics of dislocation slip obstacles, free slip distance, grains misorientation, etc. In a single phase polycrystalline alloy, slip should be activated first in soft orientation grains. When dislocations piling up at a grain boundary, dislocation-induced stress concentration should exert on the hard orientation grain and result in a back stress on the soft grain. At a certain strain, the stress concentration depends on the grain size and misorientation characterized by the geometry penetration parameter. For a randomly orientated alloy, this process was already characterized

by Hall-petch relationship, summarized as grain boundary strengthening. In the LUR stress-strain curves (Fig. 11 (b)), no obvious hysteresis loop induced by the Bauschinger effect can be found, indicating that little back stress was induced in the investigated alloys. The difference of strain hardening rate was quite limited in the same alloys with different grain sizes (see Table 1). This means that the strain hardening rate relates little to grain boundary. Consequently, it is deduced that the difference of the strain hardening rate between the investigated alloys could only results from the dislocations interaction, i.e. forest dislocation strengthening as indicated by Laplanche et al. [45], expressed as:

$$\frac{1}{V} = \frac{1}{0.55\Delta E_b M} \sigma_{ss}(T, \dot{\varepsilon}) + \frac{\beta}{M} (\sigma - \sigma_y) \quad (10a)$$

$$\beta = \frac{1}{w a' \mu b^2} \quad (11)$$

where V represents the thermally activated volume; w represents length scale of dislocation barrier, taken as lattice constant a . According to the experimental results (as seen in Fig. 11), true stress is nearly in line with

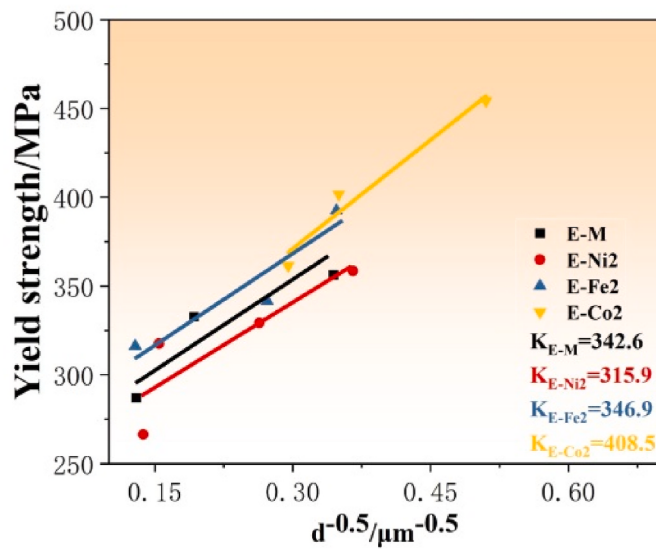


Fig. 9. Yield strength of the alloys vs. the average grain diameter.

Table 2

The values of $\underline{\delta R}_{ij}$ (left bottom with underline) and δG_{ij} (right top with bold font).

Element i/j	Cr	Fe	Co	Ni
Cr	0	0.3350	0.4211	0.4084
Fe	<u>0.0064</u>	0	0.0892	0.0759
Co	<u>-0.0016</u>	<u>-0.0080</u>	0	-0.0132
Ni	<u>0.0024</u>	<u>-0.0040</u>	<u>0.0040</u>	0

Table 3

The parameter values of δ_i and η_i .

Sample	Parameter	Cr	Fe	Co	Ni
E-M	δ_i	0.315373	0.135456	0.134599	0.127585
	η_i	0.001958	-0.00152	-0.00152	0.000647
E-Ni2	δ_i	0.34078	0.124821	0.104809	0.102068
	η_i	0.002088	-0.00209	-0.00035	0.000518
E-Fe2	δ_i	0.324887	0.108365	0.127	0.118523
	η_i	0.002959	-0.00122	-0.00296	-0.00035
E-Co2	δ_i	0.343527	0.127686	0.107679	0.099198
	η_i	0.00122	-0.00296	-0.00122	0.001385

Table 4

The parameter values included in the calculation using the Varvenne model.

Sample	$\bar{\rho}$ (GPa)	\bar{v}	$a(\text{\AA})$	$b(\text{\AA})$	M
E-M	87.0	0.273	4.05	2.864	3.10
E-Ni2	84.8	0.276	3.75	2.654	3.09
E-Fe2	86.0	0.276	3.92	2.769	3.20
E-Co2	84.6	0.278	3.77	2.667	3.19

strain. Accordingly, we used ultimate tensile strength σ_f to calculate the totally activated volume V in the whole plastic flow process in the E-M, E-Ni2, E-Fe2 and E-Co2 alloys corresponding to those in Fig. 11, of which grain size was 26.88 μm , 10.72 μm , 13.49 μm , and 11.49 μm , respectively. The calculated V is accordingly 2.04 nm^3 , 1.96 nm^3 , 1.80 nm^3 , and 1.60 nm^3 . As seen from Fig. 11, strain hardening rate is negatively correlated to activated volume. In the forest dislocation strengthening, L-C locks play an important role. The E-Fe2 and E-Co2 alloys exhibited more SFs with L-C locks (see Figs. 7 and 8) as compared with the E-M and E-Ni2 alloys (see Figs. 5 and 6). SFs are quite beneficial to strain hardening [46,47]. More SFs in the E-Co2 and E-Fe2 alloys were responsible for the higher strain hardening rate.

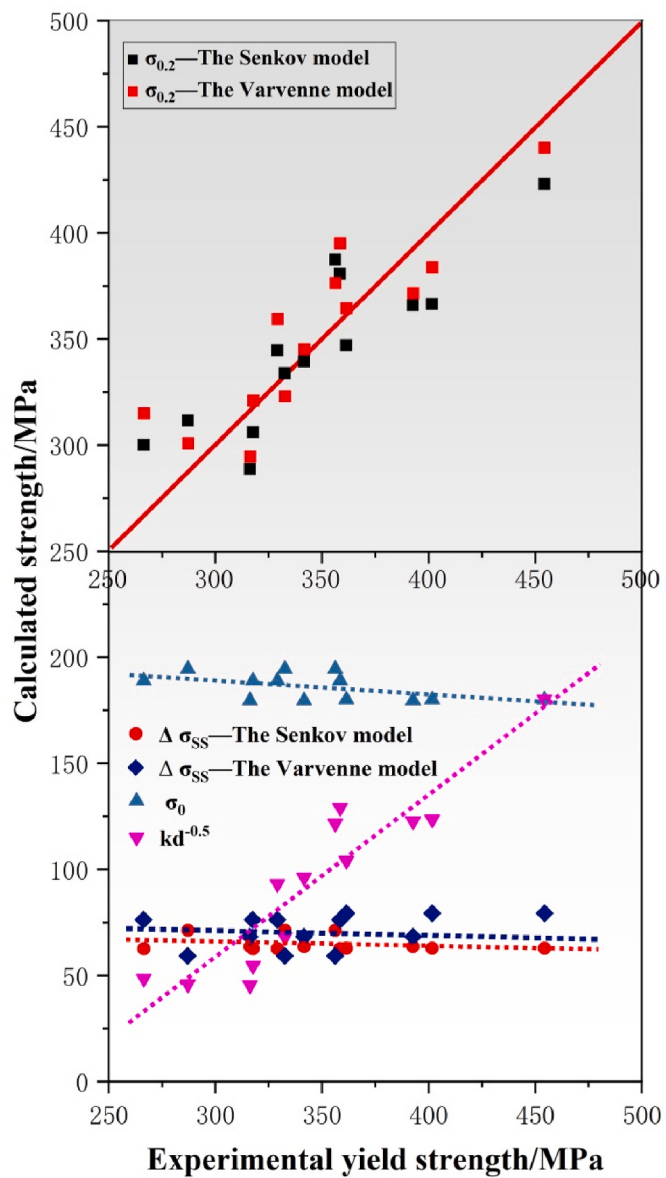


Fig. 10. The comparison of yield strengths between the experimental and calculated results.

4.3. Ductility

To identify independent parameters that influence ductility is very important. Ductility relates to intrinsic and extrinsic multi-factors. In terms of deformation mechanism and deformation process, the plastic strain rate is determined by activated dislocation density ρ , Burgers vector magnitude b , and dislocation velocity v according to the dislocation-based slip rule, $\dot{\gamma} = \rho bv$ [48]. Obviously, plastic strain depends on ρ and b (or a , $b = \frac{\sqrt{3}}{2}a$). Activated dislocation density is inverse proportional to the square of activated-volume [45]. Consequently, we deduce that in addition to lattice constant a , plastic strain depends on strain hardening rate h .

When a dislocation moves to a grain boundary, the free slip distance approximately equals the grain diameter d . Large grain size is favorable for plastic strain due to the potential long free slip distance. Small grains need high density dislocations to accommodate strain as indicated in Refs. [49–51] and the present results (see Fig. 3). GNDs (including L-C dislocations) are unmovable that would affect continuous slip in the whole deformation process. Although reducing the free slip distance,

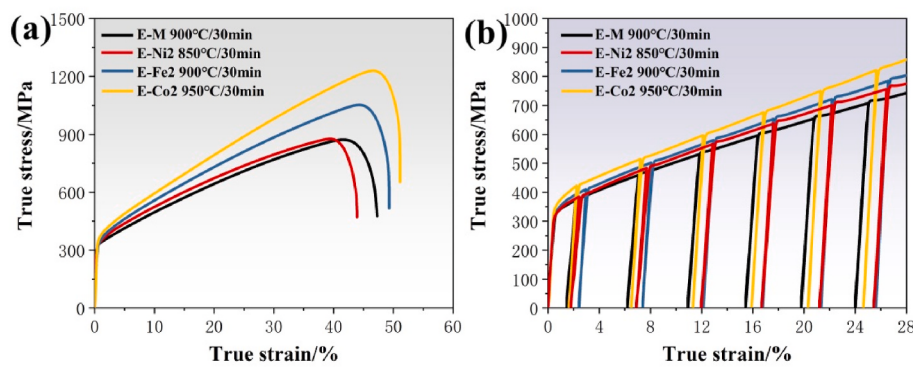


Fig. 11. True tensile stress-strain curves of the alloys. (a) Continuous tension; (b) Tension with loading-unloading-reloading.

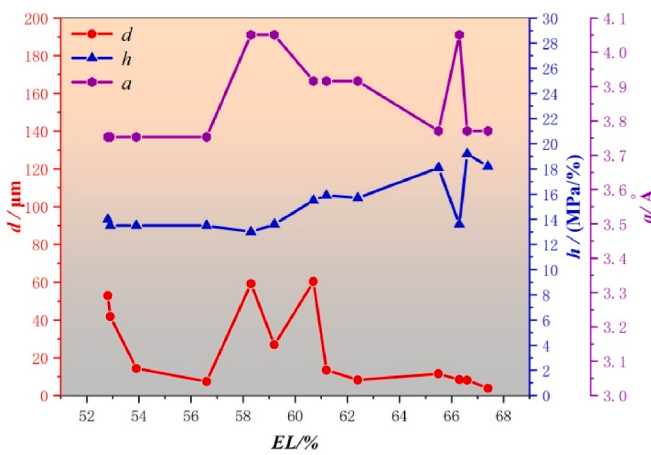


Fig. 12. Parameter variations vs. ductility (tensile elongation, EL) of the alloys.

Table 5

The ductility list in order from low to high, with the corresponding parameters.

Order number j	$El (\%) x_1^{(0)}(j)$	$d(\mu\text{m}) x_2^{(0)}(j)$	$h (\text{MPa}/\%) x_3^{(0)}(j)$	$a (\text{\AA}) x_4^{(0)}(j)$
1	52.8	52.94	14.0	3.753
2	52.9	41.84	13.5	3.753
3	53.9	14.37	13.5	3.753
4	56.6	7.48	13.5	3.753
5	58.3	59.24	13.0	4.051
6	59.2	26.88	13.6	4.051
7	60.7	60.4	15.5	3.916
8	61.2	13.49	15.9	3.916
9	62.4	8.28	15.7	3.916
10	65.5	11.49	18.1	3.771
11	66.3	8.42	13.6	4.051
12	66.6	8.16	19.2	3.771
13	67.4	3.84	18.2	3.771

GNDs benefit for strain hardening and strain hardening rate. High strain hardening rate is beneficial to homogeneous plastic deformation among grains, so that enhances ductility [52].

As discussed above, the parameters influencing ductility are multiple, covering average grain size, strain hardening rate, and Burgers vector magnitude b (or lattice constant a). Fig. 12 presents the parameter variations vs. the ductility (tensile elongation, EL) of the alloys. It can be seen that the comprehensive effect of the parameters is really nebulous. a and h are similar at the first four data points, only d decreases as EL increases. It is noted that the data at the first four points all come from the E-Ni2 alloy with different grain size. This indicates that grain refinement is favorable for enhancing ductility in terms of the increment of activated dislocation density [48–51], meanwhile the effect of GNDs

and grain size on the free slip distance could play a role. As EL increases further, the parameters fluctuates in the alloys, influencing EL comprehensively.

Considering the comprehensiveness and fuzziness of the relationship between the ductility and the physical parameters, the grey system theory is suitable for analyzing this relationship. The grey system theory was initially developed in economy, and consequently used in more research fields. It is conveniently used to analyze the system with the “grey” characteristics [53,54], in which some information is clear, while others are unknown. In this study, we analyzed the effect the parameters of average grain size d , strain hardening rate h , and lattice constant a on ductility in terms of the grey system theory. Table 5 lists the ductility values in order from low to high, and the corresponding parameters values.

To analyze the relation ship between the ductility and the parameters, we can treat the El order as a “time” series denoted by $x_1^{(0)}(j)$ according to the grey system theory. Correspondingly, the parameters are in the series of $x_2^{(0)}(j)$, $x_3^{(0)}(j)$, and $x_4^{(0)}(j)$, respectively ($j_{\max} = 13$). Consequently, we can obtain 4 groups of “time” series $x_i^{(0)}(j)$ ($i_{\max} = 4$). Normalizing these groups of series $x_i^{(0)}(j)$ by $X_i^{(0)}(j) = [x_i^{(0)}(j)-\min(x_i^{(0)}(j))]/[\max(x_i^{(0)}(j))-\min(x_i^{(0)}(j))]$, we obtained new groups of series data $X_i^{(0)}(j)$. Based on the normalized data, three groups of differential value series can be obtained by

$$\Delta X_{i-1}^{(0)}(j) = |X_1^{(0)}(j) - X_i^{(0)}(j)| \quad (i=2, 3, 4) \quad (8b)$$

Consequently, the correlation coefficient of parameters with ductility can be estimated by

$$\varepsilon_{i-1}(j) = \frac{\Delta(\min) + \sigma}{\Delta X_{i-1}^{(0)}(j) + \sigma} \quad (9b)$$

where $\Delta(\min) = \min \{ \Delta X_{i-1}(\min) \}$, $\Delta X_{i-1}(\min) = \min \{ \Delta X_{i-1}^{(0)}(j) \}$; $\sigma = 0.5\Delta(\max)$, $\Delta(\max) = \max \{ \Delta X_{i-1}(\max) \}$, $\Delta X_{i-1}(\max) = \max \{ \Delta X_{i-1}^{(0)}(j) \}$. Finally, the grey correlation degree can be determined by

$$r_{i-1} = \frac{1}{n} \sum_{j=1}^n \varepsilon_{i-1}(j) \quad (n=13) \quad (10b)$$

The grey correlation degree is a measure of the influence of various parameters on the ductility. The calculated grey correlation degree of d , h and a is 0.52, 0.75 and 0.70, respectively. The correlation order is $r_h > r_a > r_d$. This means that the dominant parameter is h . The high ductility of the E-Co2 alloy was mainly attributed to the high hardening rate. The high strain hardening rate results from forest strengthening, promoted by SFs with L-C locks. Because of lacking SFs, the E-Ni2 alloy had the lowest ductility. In addition, the activated volume in the E-Ni2 alloy was larger as compared with that in the E-Co2 or E-Fe2 alloy, which is unfavorable for ductility. The effect of grain size d is multiplicative. It is beneficial for high dislocation density, but unfavorable for the free slip

distance. Therefore, Co-enrichment could be more favorable for the strength-ductility enhancement of the solid-solution matrix in Ni–Fe–Co–Cr HEAs with high strain hardening rate and small activated volume.

5. Conclusions

- (1) The recrystallization progresses more slowly in the NiFeCo₂Cr alloy than in the E-M, E-Ni2 and E-Fe2 alloys. Under the same heat treatment condition, the NiFeCo₂Cr alloy exhibits finer grains. The recrystallization process is the fastest in the Ni₂Fe-CoCr alloy.
- (2) Adjusting the elemental proportions in Ni–Fe–Co–Cr HEAs for strengthening is inefficient, because the solid-solution strengthening by atomic radius mismatch/the misfit volume, Burgers vector magnitude, shear modulus, and shear modulus mismatch is quite similar in the different molar ratio alloys. The strengthening of the alloys mainly depends on grain refinement.
- (3) The strain hardening rate has the dominant influence on the ductility of the alloys. The NiFeCo₂Cr and NiFe₂CoCr alloys exhibit higher strain hardening rate than the NiFeCoCr and Ni₂FeCoCr alloys. The higher strain hardening rate of the NiFeCo₂Cr and NiFe₂CoCr alloys dominantly results from forest dislocation strengthening promoted by the activated stacking faults with Lomer-Cottrell locks.
- (4) According to the analysis in terms of the system theory, the lattice constant have a certain effect on the ductility.

CRediT authorship contribution statement

Jiale Man: Investigation, Formal analysis, Data curation. **Baolin Wu:** Writing – review & editing, Supervision, Project administration, Methodology, Funding acquisition, Conceptualization. **Guosheng Duan:** Investigation, Formal analysis. **Lu Zhang:** Formal analysis, Data curation. **Yandong Liu:** Supervision, Resources. **Claude Esling:** Writing – review & editing, Supervision.

Declaration of competing interest

I write on behalf of myself and all co-authors to declare that the authors have no known competing financial interests or personal relationships that could have appeared to influence the work reported in this paper.

Data availability

The data that has been used is confidential.

Acknowledgments

The authors gratefully acknowledge the financial support from the National Natural Science Foundation of China (No. 51371121).

References

- [1] Cheng Zhang, Qin Yu, Yuanbo T. Tang, Mingjie Xu, Haoren Wang, Chaoyi Zhu, Jon Ell, Shiteng Zhao, Benjamin E. MacDonald, Penghui Cao, Julie M. Schoenung, Kenneth S. Vecchio, Roger C. Reed, Robert O. Ritchie, Enrique J. Lavernia, Strong and ductile FeNiCoAl-based high-entropy alloys for cryogenic to elevated temperature multifunctional applications, *Acta Mater.* 242 (2023) 118449.
- [2] Zezhou Li, Shiteng Zhao, Robert O. Ritchie, Marc A. Meyers, Mechanical properties of high-entropy alloys with emphasis on face-centered cubic alloys, *Prog. Mater. Sci.* 102 (2019) 296–345.
- [3] Mingliang Wang, Yiping Lu, Jinggang Lan, Tongmin Wang, Chuan Zhang, Zhiqiang Cao, Tingju Li, Peter K. Liaw, Lightweight, ultrastrong and high thermal-stable eutectic high-entropy alloys for elevated-temperature applications, *Acta Mater.* 248 (2023) 118806.
- [4] Mingliang Wang, Yiping Lu, Guojia Zhang, Hongzhi Cui, Dingfeng Xu, Na Wei, Tingju Li, A novel high-entropy alloy composite coating with core-shell structures prepared by plasma cladding, *Vacuum* 184 (2021) 109905.
- [5] Liang Wei, Wei-Min Qin, Jing-Yao Chen, Wen-Xin Lei, Jin-Yang Xi, L₂₁-strengthened face-centered cubic high-entropy alloy with well pitting resistance, *Corrosion Sci.* 215 (2023) 111043.
- [6] Y. Zhang, T. Ting, Z. Tang, M.C. Gao, K.A. Dahmen, P.K. Liaw, Z. Ping, Progress in materials science microstructures and properties of high-entropy alloys, *Prog. Mater. Sci.* 61 (2014) 1–93.
- [7] B. Gludovatz, A. Hohenwarter, D. Catoor, E.H. Chang, E.P. George, R.O. Ritchie, A fracture-resistant high-entropy alloy for cryogenic applications, *Science* 345 (2014) 1153–1158.
- [8] D.B. Miracle, O.N. Senkov, A critical review of high entropy alloys and related concepts, *Acta Mater.* 122 (2017) 448–511.
- [9] Jiasheng Wang, Yujiao Ke, Yifei Chen, Chenjing Li, Tonggang Lu, Xingang Liu, Zhefeng Xu, Wenwen Zhang, Hu Tang, Cheng Guo, Kazuhiro Matsugi, Microstructural mechanisms imparting high strength-ductility synergy in heterogeneous structured as-cast AlCoCrFeNi_{2.1} eutectic high-entropy alloy, *J. Mater. Res. Technol.* 27 (2023) 8119–8131.
- [10] H.M. Daoud, A. Manzoni, R. Volk, N. Wandler, U. Glatzel, Microstructure and tensile behavior of Al₈Co₁₇Cr₁₇Cu₈Fe₁₇Ni₃₃ (at.%) high-entropy alloy, *J. Occup. Med.* 65 (2013) 1805–1814.
- [11] D.G. Shaysultanov, N.D. Stepanov, A.V. Kuznetsov, G.A. Salishchev, O.N. Senkov, Phase composition and superplastic behavior of a wrought AlCoCrCuFeNi high-entropy alloy, *J. Occup. Med.* 65 (2013) 1815–1828.
- [12] Longfei Zeng, Luming Zeng, Peng Xu, Weijiang Liu, Tongxiang Liang, Weirong Li, Xuehui Zhang, Enhanced strength-ductility synergy in high-entropy alloys via architecting three-level gradient hierarchical nanostructure, *Mater. Sci. Eng., A* 885 (2023) 145597.
- [13] Z. Wu, H. Bei, G.M. Pharr, E.P. George, Temperature dependence of the mechanical properties of equiatomic solid solution alloys with face-centered cubic crystal structures, *Acta Mater.* 81 (2014) 428–441.
- [14] Mingliang Wang, Hongzhi Cui, Yong Zhao, Canming Wang, Na Wei, Xiaohua Gao, Qiang Song, Enhanced strength and ductility in a spark plasma sintered CoCrCu_{0.5}NiAl_{0.5} high-entropy alloy via a double-step ball milling approach for processing powders, *Mater. Sci. Eng., A* 762 (2019) 138071.
- [15] Xinlei Miao, Gang Liu, Cuicui Xu, Daoyu Wang, Zhenhua Han, Guojun Zhang, Achieving strength and ductility synergy in (CoCrFeNi)₄Ti₂Al high entropy alloy with multi-scale heterogeneous microstructure, *Intermetallics* 164 (2024) 108107.
- [16] X.H. Du, W.P. Li, H.T. Chang, T. Yang, G.S. Duan, B.L. Wu, J.C. Huang, F.R. Chen, C.T. Liu, W.S. Chuang, Y. Lu, M.L. Sui, E.W. Huang, Dual heterogeneous structures lead to ultrahigh strength and uniform ductility in a Co-Cr-Ni medium-entropy alloy, *Nat. Commun.* 11 (2020) 2390.
- [17] Lei Fan, Tao Yang, Yiliu Zhao, Junhua Luan, Gang Zhou, Hao Wang, Zengbao Jiao, Chain-Tsuan Liu, Ultrahigh strength and ductility in newly developed materials with coherent nanolamellar architectures, *Nat. Commun.* 11 (2020) 6240.
- [18] Baolin Wu, Jiale Man, Guosheng Duan, Lu Zhang, Xinghao Du, Yandong Liu, Claude Esling, Constructing a heterogeneous microstructure in the CoCrFeNi-based high entropy alloy to obtain a superior strength-ductility synergy, *Mater. Sci. Eng., A* 886 (2023) 145669.
- [19] R.L. Fleischman, Solution hardening, *Acta Metall.* 9 (1961) 996–1000.
- [20] R.L. Fleischman, Substitutional solution hardening, *Acta Metall.* 11 (1963) 203–209.
- [21] R. Labusch, A Statistical Theory of solid solution hardening, *Phys. Status Solidi* 41 (1970) 659–669.
- [22] O.N. Senkov, J.M. Scott, S.V. Senkova, D.B. Miracle, C.F. Woodward, Microstructure and room temperature properties of a high-entropy TaNbHfZrTi alloy, *J. Alloys Compd.* 509 (2011) 6043–6048.
- [23] Céline Varvenne, Aitor Luque, William A. Curtin, Theory of strengthening in fcc high entropy alloys, *Acta Mater.* 118 (2016) 164–176.
- [24] C. Varvenne, G.P.M. Leyson, M. Ghazisaeidi, W.A. Curtin, Solute strengthening in random alloys, *Acta Mater.* 124 (2017) 660–683.
- [25] Francesco Maresca, William A. Curtin, Theory of screw dislocation strengthening in random BCC alloys from dilute to “High Entropy” alloys, *Acta Mater.* 182 (2020) 144–162.
- [26] S.R. Reddy, S. Yoshida, T. Bhattacharjee, N. Sake, A. Lozinko, S. Guo, P. Bhattacharjee, N. Tsuji, Nanostructuring with Structural-Compositional dual heterogeneities enhances Strength-Ductility synergy in eutectic high entropy alloy, *Sci. Rep.* 9 (2019) 1–9.
- [27] Y.H. Jo, S. Jung, W.M. Choi, S.S. Sohn, H.S. Kim, B.J. Lee, N.J. Kim, S. Lee, Cryogenic strength improvement by utilizing room-temperature deformation twinning in a partially recrystallized VCrMnFeCoNi high-entropy alloy, *Nat. Commun.* 8 (2017) 15719.
- [28] J.Y. He, H. Wang, Y. Wu, X.J. Liu, H.H. Mao, T.G. Nieh, Z.P. Lu, Precipitation behavior and its effects on tensile properties of FeCoNiCr high-entropy alloys, *Intermetallics* 79 (2016) 41–52.
- [29] Feng He, Da Chen, Bin Han, Qingfeng Wu, Zhipun Wang, Shaolou Wei, Daixiu Wei, Jincheng Wang, C.T. Liu, Ji-jung Kai, Design of D₀₂₂ superlattice with superior strengthening effect in high entropy alloys, *Acta Mater.* 167 (2019) 275–286.
- [30] M. Ashby, The deformation of plastically non-homogeneous materials, *The Philosophical Magazine: A Journal of Theoretical Experimental and Applied Physics* 21 (1970) 399–424.
- [31] E. Song, M.T. Andani, A. Misra, Investigation of grain size and geometrically necessary dislocation density dependence of flow stress in Mg-4Al by using nanoindentation, *Acta Mater.* 265 (2023) 119633.
- [32] L. Evers, W. Brekelmans, M. Geers, Non-local crystal plasticity model with intrinsic SSD and GND effects, *J. Mech. Phys. Solid.* 52 (2004) 2379–2401.

- [33] G.D. Sathiaraj, M.Z. Ahmed, P.P. Bhattacharjee, Microstructure and texture of heavily cold-rolled and annealed fcc equiatomic medium to high entropy alloys, *J. Alloys Compd.* 664 (2016) 109–119.
- [34] Lalit Kaushik, Min-Seong Kim, Jaiveer Singh, Joo-Hee Kang, Yoon-Uk Heo, Jin-Yoo Suh, Shi-Hoon Choi, Deformation mechanisms and texture evolution in high entropy alloy during cold rolling, *Int. J. Plast.* 141 (2021) 102989.
- [35] S. Paul, B. Tripathy, R. Saha, P.P. Bhattacharjee, Microstructure and texture of heavily cold-rolled and annealed extremely low stacking fault energy Cr₂₆Mn₂₀Fe₂₀Co₂₀Ni₁₄ high entropy alloy: comparative insights, *J. Alloys Compd.* 930 (2023) 167418.
- [36] P.P. Bhattacharjee, G.D. Sathiaraj, M. Zaid, J.R. Gatti, Chi Lee, Che-Wei Tsai, Jian-Wei Yeh, Microstructure and texture evolution during annealing of equiatomic CoCrFeMnNi high-entropy alloy, *J. Alloys Compd.* 587 (2014) 544–552.
- [37] Lalit Kaushik, Jaiveer Singh, Joo-Hee Kang, Yoon Seok Ko, Dong-Ik Kim, Jin-Yoo Suh, Shi-Hoon Choi, Deciphering the role of multiple generations of annealing twins on texture evolution in cold-rolled high entropy alloys during annealing, *Scripta Mater.* 205 (2021) 114221.
- [38] Baoqi Guo, Ranjit K. Ray, Shuhei Yoshida, Yu Bai, Nobuhiro Tsuji, In-situ observations of static recrystallization and texture formation in a cold-rolled CoCrFeMnNi high entropy alloy, *Scripta Mater.* 215 (2022) 114706.
- [39] G. Dan Sathiaraj, Aurimas Pukenas, Werner Skrotzki, Texture formation in face-centered cubic high-entropy alloys, *J. Alloys Compd.* 826 (2020) 154183.
- [40] L. Dupuy, M.C. Fivel, A study of dislocation junctions in FCC metals by an orientation dependent line tension model, *Acta Mater.* 50 (2002) 4873–4885.
- [41] Qian Wang, Bing Wang, Weifeng Yuan, Bin Gu, Probing the crystal structure and dislocation evolution in single crystal Al_{0.3}CoCrFeNi high-entropy alloy under nanoindentation, *Mater. Today Commun.* 34 (2023) 104983.
- [42] Céline Varvenne, William A. Curtin, Predicting yield strengths of noble metal high entropy alloys, *Scripta Mater.* 142 (2018) 92–95.
- [43] Dingfeng Xu, Haitao Zhang, Mingliang Wang, Yiping Lu, Xiaohu Chen, Zheng Ren, Enhanced strength-ductility synergy in a Ta-doped CoCrNi medium-entropy alloy with a dual heterogeneous structure, *Mater. Sci. Eng., A* 860 (2022) 144293.
- [44] Z. Cheng, H. Zhou, Q. Lu, H. Gao, L. Lu, Extra strengthening and work hardening in gradient nanotwinned metals, *Science* 362 (2018) eaau1925.
- [45] G. Laplanche, J. Bonneville, C. Varvenne, W.A. Curtin, E.P. George, Thermal activation parameters of plastic flow reveal deformation mechanisms in the CrMnFeCoNi high-entropy alloy, *Acta Mater.* 143 (2018) 257–264.
- [46] M. Frank, S.S. Nene, Y. Chen, S. Thapliyal, S. Shukla, K. Liu, S. Sinha, T. Wang, M. J. Frost, K. An, R.S. Mishra, Direct evidence of the stacking fault-mediated strain hardening phenomenon, *Appl. Phys. Lett.* 119 (2021) 081906.
- [47] Sijing Chen, Hyun Seok Oh, Bernd Gludovatz, Sang Jun Kim, Eun Soo Park, Ze Zhang, Robert O. Ritchie, Real-time observations of TRIP-induced ultrahigh strain hardening in a dual-phase CrMnFeCoNi high-entropy alloy, *Nat. Commun.* 11 (2020) 826.
- [48] D. Hull, D.J. Bacon, *Introduction to Dislocations*, fifth ed., 2011, pp. 59–62, 3.
- [49] Morton E. Gurtin, Nobutada Ohno, A gradient theory of small-deformation, single-crystal plasticity that accounts for GND-induced interactions between slip systems, *J. Mech. Phys. Solid.* 59 (2011) 320–343.
- [50] Francisco Cruz-Gandarilla, Ana María Salcedo-Garrido, Raúl E. Bolmaro, Thierry Baudin, Natalia S. De Vincentis, Martina Avalos, José G. Cabañas-Moreno, Héctor Mendoza-León, Microstructural evolution and mechanical properties on an ARB processed IF steel studied by X-ray diffraction and EBSD, *Mater. Char.* 118 (2016) 332–339.
- [51] C. Reuber, P. Eisenlohr, F. Roters, D. Raabe, Dislocation density distribution around an indent in single-crystalline nickel: comparing nonlocal crystal plasticity finite-element predictions with experiments, *Acta Mater.* 71 (2014) 333–348.
- [52] Z.H. Cao, G.Y. Zhai, Y.J. Ma, L.P. Ding, P.F. Li, H.L. Liu, H.M. Lu, Y.P. Cai, G. J. Wang, X.K. Meng, Evolution of interfacial character and its influence on strain hardening in dual-phase high entropy alloys at nanoscale, *Int. J. Plast.* 145 (2021) 103081.
- [53] Wanli Xie, Wen-Ze Wu, Zhenguo Xu, Caixia Liu, Keyun Zhao, The fractional neural grey system model and its application, *Appl. Math. Model.* 121 (2023) 43–58.
- [54] Huiping Wang, Zhun Zhang, A spatial lagged multivariate discrete grey model for forecasting an economy-energy-environment system, *J. Clean. Prod.* 404 (2023) 136922.